



## Synthesis and properties of hydroxyapatite-containing porous titania coating on ultrafine-grained titanium by micro-arc oxidation

Z.Q. Yao<sup>a,b,\*</sup>, Yu. Ivanisenko<sup>c</sup>, T. Diemant<sup>d</sup>, A. Caron<sup>b</sup>, A. Chuvilin<sup>e</sup>, J.Z. Jiang<sup>f,g</sup>, R.Z. Valiev<sup>h</sup>, M. Qi<sup>a,\*</sup>, H.-J. Fecht<sup>b,c,\*</sup>

<sup>a</sup> School of Materials Science and Engineering, Dalian University of Technology, Dalian 116024, People's Republic of China

<sup>b</sup> Institute of Micro and Nanomaterials, Ulm University, Ulm 89081, Germany

<sup>c</sup> Institute of Nanotechnology, Karlsruhe Institute of Technology, Karlsruhe 76021, Germany

<sup>d</sup> Institute of Surface Chemistry and Catalysis, Ulm University, Ulm 89069, Germany

<sup>e</sup> Central Facility of Electron Microscopy, Ulm University, Ulm 89069, Germany

<sup>f</sup> International Center for New-Structured Materials (ICNSM), Zhejiang University, Hangzhou 310027, People's Republic of China

<sup>g</sup> Laboratory of New-Structured Materials, Department of Materials Science and Engineering, Zhejiang University, Hangzhou 310027, People's Republic of China

<sup>h</sup> Institute of Physics of Advanced Materials, Ufa State Aviation Technical University, Ufa 450000, Russian Federation

### ARTICLE INFO

#### Article history:

Received 18 October 2009

Received in revised form 21 December 2009

Accepted 30 December 2009

Available online 4 January 2010

#### Keywords:

Micro-arc oxidation

Equal channel angular pressing

Coating

Ultrafine-grained titanium

Nanocrystalline hydroxyapatite

### ABSTRACT

Equal channel angular pressing results in ultrafine-grained ( $\sim 200$ – $500$  nm) Ti with superior mechanical properties without harmful alloying elements, which benefits medical implants. To further improve the bioactivity of Ti surfaces, Ca/P-containing porous titania coatings were prepared on ultrafine-grained and coarse-grained Ti by micro-arc oxidation (MAO). The phase identification, composition, morphology and microstructure of the coatings and the thermal stability of ultrafine-grained Ti during MAO were investigated subsequently. The amounts of Ca, P and the Ca/P ratio of the coatings formed on ultrafine-grained Ti were greater than those on coarse-grained Ti. Nanocrystalline hydroxyapatite and  $\alpha$ -Ca<sub>3</sub>(PO<sub>4</sub>)<sub>2</sub> phases appeared in the MAO coating formed on ultrafine-grained Ti for 20 min (E20). Incubated in a simulated body fluid, bone-like apatite was completely formed on the surface of E20 after 2 days, thus evidencing preferable bioactivity. Compared with initial ultrafine-grained Ti, the microhardness of the E20 substrate was reduced by 8% to 2.9 GPa, which is considerably more than that of coarse-grained Ti ( $\sim 1.5$  GPa).

© 2010 Acta Materialia Inc. Published by Elsevier Ltd. All rights reserved.

### 1. Introduction

Commercial pure titanium and its alloys have been widely utilized in the biomedical field because of their exceptional biocompatibility, low elastic modulus, excellent corrosion resistance and high strength-to-density ratio. Titanium alloys (e.g. Ti6Al4V) are generally used for orthopedic and dental implants more frequently than commercial pure titanium due to their superior mechanical strength [1]. However, such elements as aluminum and vanadium may be harmful to the human body, thus restricting further biomedical applications of Ti6Al4V alloy [2,3].

Grain refinement is an effective method to enhance the mechanical strength without the need of adding a potentially harmful alloying element [4,5]. Ultrafine-grained (UFG) metals and alloys processed by severe plastic deformation techniques, e.g. high pressure torsion [6,7], cyclic extrusion compression [8] and equal channel angular pressing (ECAP) [9,10], show superior mechanical properties, such as high strength and improved ductil-

ity, as well as lower temperature and higher strain rate superplasticity. Among all the severe plastic deformation techniques, the ECAP technique is especially attractive because it can economically produce bulk UFG materials that are 100% dense, contamination free, large enough for real structural application and with an invariant chemical composition [9–12]. It was shown recently that the microstructure of coarse-grained (CG) Ti can be significantly refined through the ECAP process and the resulting strength was enhanced from 463 to 1050 MPa [9]. This is even higher than that of the commercial Ti6Al4V alloys (950 MPa) that are generally used for implants. Moreover, very recent experimental results indicate that the grain refinement of Ti further promotes bone tissue growth and cell adhesion [13–15]. Thus, UFG pure Ti, with high strength and better biocompatibility, seems to be favorable for future applications as a biomaterial.

The pure Ti surface is covered with a thin native oxide layer, which is bioinert. After implantation, the surface is generally encapsulated by fibrous tissue without producing any osseous junctions with the surrounding tissues. Therefore, various surface-modification techniques have been developed in the past in order to improve the bioactivity and bioconductivity of Ti implants.

\* Corresponding authors. Tel.: +49 7315025492.

E-mail address: [yaozaiqi@gmail.com](mailto:yaozaiqi@gmail.com) (Z.Q. Yao).

These processes are generally divided into physical (e.g. plasma spraying and ion implanting), chemical (e.g. sol–gel routes, alkali heating and hydrothermal treatment) and electrochemical methods (e.g. anode oxidation and micro-arc oxidation (MAO)) [16–23]. The method of MAO has emerged only recently, and can produce a porous, rough and firmly adherent titania film on the titanium surface [24–27]. This process combines electrochemical oxidation with a high voltage spark treatment in an aqueous electrolytic bath containing Ca and P elements in the dissolved salts. The presence of Ca and P ions in the porous titania coating layer can further enhance the bonding between the implants and the bone with anchorage. In previous studies, the oxide coating included Ca- and P-containing phases such as typically  $\text{CaTiO}_3$ ,  $\alpha\text{-Ca}_3(\text{PO}_4)_2$ ,  $\beta\text{-Ca}_2\text{PO}_7$ ,  $\text{CaCO}_3$ ,  $\text{CaO}$  or amorphous apatite [28–30]. However, further work on MAO is still needed to improve the bio-activity of the titania coating [27,31]. A number of effective solving routines have been developed, such as hydrothermal treatment or heat treatment of the coatings to form hydroxyapatite (HA) layers on the titania [32–34].

It is well known that grain boundaries may act as fast atomic diffusion channels, and various kinds of non-equilibrium structural defects can accelerate the chemical activity of the UFG materials [35]. Thus, the use of ECAP-treated Ti as a substrate for bioactive coatings may represent an additional advantage over its conventional coarse-grained counterpart. In the present work, we used the ECAP technique to prepare a UFG commercially pure Ti sample. The as-prepared samples were coated by Ca/P-containing titania layer via the MAO process. The thickness, phase, composition and morphology of the titania layer on the two kinds of substrate were investigated as a function of MAO reaction time and the resulting bioactivities.

## 2. Materials and methods

### 2.1. Fabrication of ECAP-treated Ti specimen

Commercially pure Ti (>99.5 wt.%, Grade 2) with an average grain size of 20  $\mu\text{m}$  was used as the starting material. Pure Ti billets, 20 mm in diameter and 100 mm in length, were processed by ECAP for eight passes at a rate of 6  $\text{mm s}^{-1}$  at 450 °C, as described in Ref. [9]. These processing parameters were optimized for the best combination of ductility and efficiency in grain refinement [9].

### 2.2. Preparation of two sorts of substrates

The ECAP-treated bulk Ti samples with a diameter of typically 20 mm and a thickness of 3 mm were used as the substrates for the MAO process. Prior to MAO treatment, the surface of the samples was ground using 1200# abrasive paper and ultrasonically cleaned with a succession of acetone, ethyl alcohol and distilled water. For comparison, the starting CG Ti plates were treated in the same way.

### 2.3. Synthesis of MAO coatings

A 2 kW alternating current MAO device was used to fabricate ceramic coatings. A mixed aqueous solution containing 0.1  $\text{mol l}^{-1}$  calcium acetate monohydrate ( $(\text{CH}_3\text{COO})_2\text{Ca}\cdot\text{H}_2\text{O}$ , AR) and 0.06  $\text{mol l}^{-1}$  sodium dihydrogen phosphate ( $\text{NaH}_2\text{PO}_4\cdot 2\text{H}_2\text{O}$ , AR) was used as the electrolyte, and a flat stainless-steel plate was used as cathode. The MAO process was conducted at a fixed applied voltage of about 550 V using a pulse power supply for 2, 5, 10 and 20 min. The frequency and duty cycle were fixed at 600 Hz and 10%, respectively. Due to the anisotropy of ECAP-treated Ti

samples, MAO coatings were prepared on the cross-section of ECAP-treated samples here. After MAO treatments, the specimens were washed with distilled water. The ECAP samples treated for 2, 5, 10 and 20 min were named as series E: E02, E05, E10 and E20, respectively. Accordingly, the CG substrate samples were named as series C: C02, C05, C10 and C20.

### 2.4. Characterization of microstructure and composition of oxide layer

The phase composition of the coatings was analyzed by X-ray diffraction (XRD; X'pert PRO) using  $\text{Co K}\alpha$  radiation at 40 kV and 30 mA with a scanning speed of 4°/min and a step size of 0.02°. The surface and cross-sectional morphology of the coatings were examined by scanning electron microscopy (SEM; LEO 1530 field emission gun SEM). The mean elemental composition of each coating surface was analyzed with energy dispersive X-ray spectrometer (EDX) incorporated into the scanning electron microscope using the “area scanning” mode. The microstructure of the substrates for the sample in the extension direction, before and after MAO processing for 20 min, was observed by automated indexing of the electron backscattered diffraction (EBSD) patterns.

X-ray photoelectron spectroscopy (XPS; 5800 Multi Technique ESCA system) was used to determine the chemical compositions and chemical states of the coatings in a depth range of ~5 nm. In the XPS experiment, a monochromatic  $\text{Al K}\alpha$  (1486.6 eV) X-ray source was used with an anode power of 250 W. A region of  $0.4 \times 0.4 \text{ mm}^2$  on each sample surface was analyzed with a hemispherical analyzer using pass energies of 187.85 eV for survey spectra and 29.35 eV for detail spectra. The measured binding energies were calibrated by the C1s (hydrocarbons) at 284.8 eV.

The microstructure of E20 cross-sectional sample was observed by transmission electron microscopy (TEM; Philips EM 301) at an accelerating voltage of 120 kV. The TEM foils were prepared by low-angle Ar-ion milling.

### 2.5. Nanoindentation test

A nanoindentation testing system (Nanoindenter XP, MTS Inc.) with a well-calibrated Berkovich diamond indenter was employed to determine the elastic modulus and hardness of the Ti substrate and the MAO coating. The load resolution was about 50 nN and the displacement resolution was approximately 100 nm. All continuous stiffness measurements were carried out under the displacement control mode with a tip-displacement rate of 10  $\text{nm s}^{-1}$ .

### 2.6. Bioactivity evaluation of MAO coatings

The MAO samples were incubated in 500 ml of simulated body fluid (SBF) for 2, 4 and 8 days at 37 °C to evaluate their bioactivity. The SBF was prepared by dissolving reagent-grade NaCl,  $\text{NaHCO}_3$ , KCl,  $\text{K}_2\text{HPO}_4\cdot 3\text{H}_2\text{O}$ ,  $\text{MgCl}_2\cdot 6\text{H}_2\text{O}$ ,  $\text{CaCl}_2$  and  $\text{Na}_2\text{SO}_4$  in deionized water and buffering at pH 7.40 with tris-hydroxymethylaminomethane ( $(\text{CH}_2\text{OH})_3\text{CNH}_2$ ) and 1.0  $\text{mol l}^{-1}$  HCl at 37 °C [36]. The SBF was refreshed every 2 days so that apatite formation would not be inhibited by a lack of ions. After the test, samples were washed with distilled water and then air dried.

## 3. Experimental results

### 3.1. Surface morphologies and cross-sectional views of MAO coating layer

The SEM micrographs illustrating the progressive growth and morphology of MAO coatings on UFG Ti and CG Ti substrates are



presented in Fig. 1(a–d) and (e–h), respectively. The MAO coating contains two types of pores: micropores and submicropores.

The micropores had a roughly circular or elliptical shape like volcanic vent. Such pores were formed during the micro-arc discharge process. The change in the amount and size of the pores ( $\geq 1.0 \mu\text{m}$ ) produced on the surface with increasing time of treatment is shown in Fig. 2. After 2 min exposure, pores with maximum diameters of about 5.2 and 2.7  $\mu\text{m}$  and densities near 0.013 and 0.018 pores  $\mu\text{m}^{-2}$  (over an average area of  $150 \times 110 \mu\text{m}^2$  on each sample) are homogeneously dispersed on the coating surface of the UFG Ti (Fig. 1a) and CG Ti (Fig. 1e), respectively. The size distribution is broader for E02 than C02. As the

time increases, it is clearly seen that the diameter of such pores and the surface roughness increase accordingly (see Fig. 1b and c). As shown in Fig. 1d, after treatment for 20 min, the diameter of the largest pores is approximately 13  $\mu\text{m}$ , and many smaller pores are present. The density of the pores decreases to 0.008 pores  $\mu\text{m}^{-2}$ . Compared with the MAO coating formed on the UFG Ti, the roughness, discharge channel diameter and thickness of the coating formed on the CG Ti are significantly smaller after the same reaction time (see Fig. 1f and g). As the reaction time increases to 20 min, the pore density decreases to 0.01 pores  $\mu\text{m}^{-2}$  and the maximum diameter of the pores is about 7  $\mu\text{m}$ .

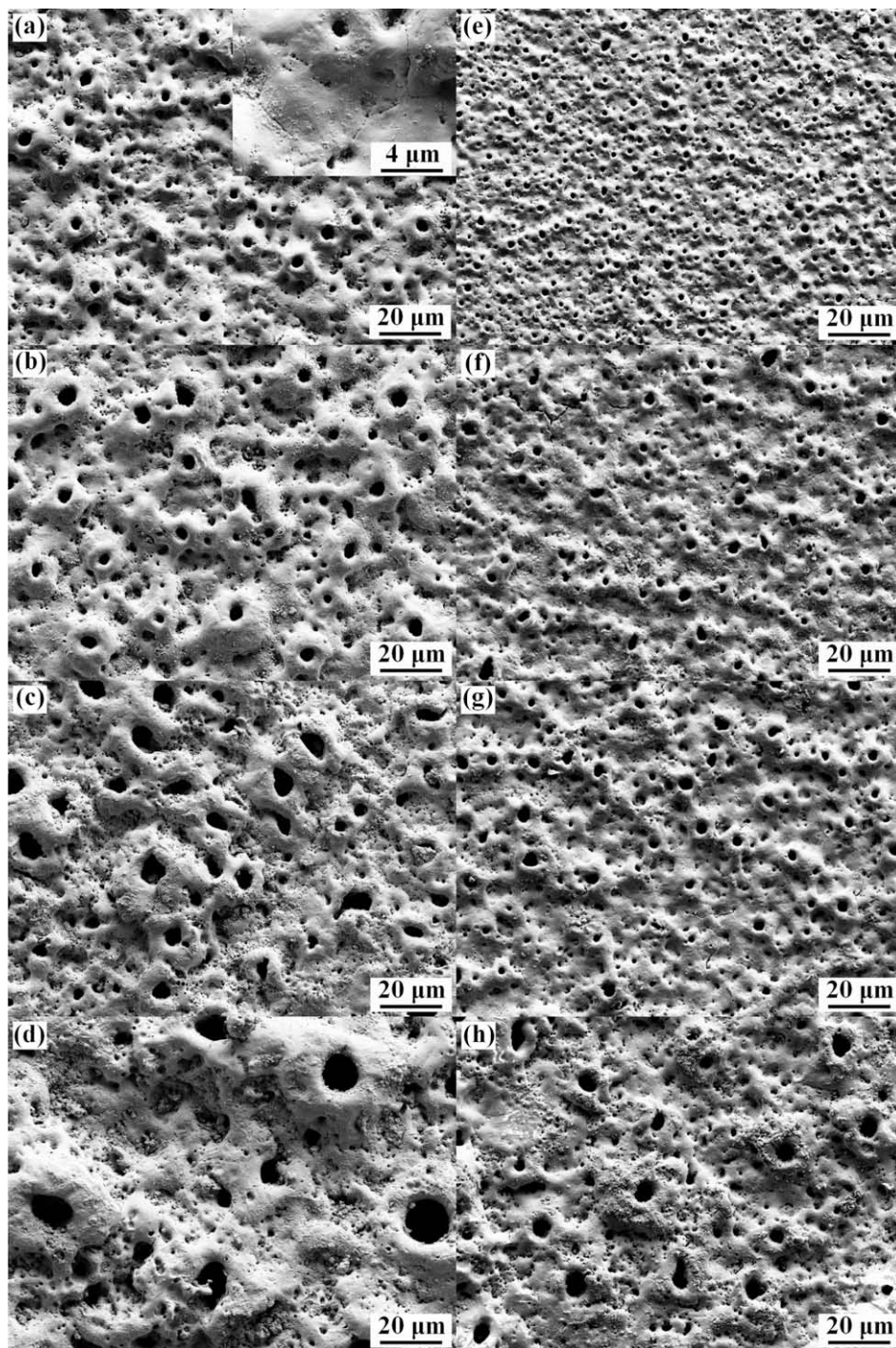


**Fig. 1.** Surface morphologies of MAO coatings formed on UFG Ti and on CG Ti. (a) E02, (b) E05, (c) E10, (d) E20, (e) C02, (f) C05, (g) C10, (h) C20.

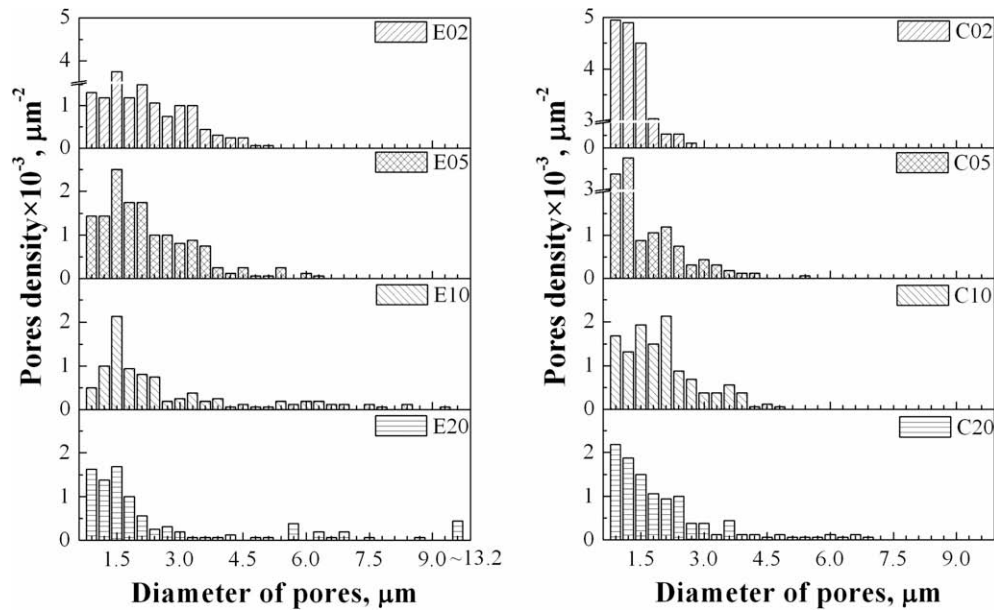


Fig. 2. Variation in micropore density vs. diameter of pores formed on UFG Ti and CG Ti during different reaction times.

Along with the micropores, some pores of submicrometer size (i.e. 0.1–1.0  $\mu\text{m}$ , see inset of Fig. 1a) can be also found. They were formed either during anodizing or at the beginning of the MAO process. The porosity of the coating layer is also increased. The porosities of the E02, E05, E10 and E20 coating surface are 5.4%, 6.7%, 7.6% and 9.5%, which are higher than the 2.7%, 3.0%, 4.4% and 5.2% of the coating formed on the CG Ti with the same reaction time.

Fig. 3 shows cross-sectional SEM views of the MAO coating layers formed on UFG Ti and CG Ti. The coating layer of each sample consists of two parts: the compact diffusion layer in contact with the substrate and the external porous conversion region containing discharge channels. The average thickness of the diffusion layer remains constant during the processing. However, with the reaction time increasing from 2 to 20 min, the average thickness of the external porous conversion layer increases from  $10 \pm 1$  to  $58 \pm 10$   $\mu\text{m}$  for UFG Ti and from  $6 \pm 1$  to  $20 \pm 5$   $\mu\text{m}$  for CG Ti (Fig. 3).

### 3.2. Coating composition

The elemental compositions of the MAO coating surfaces were analyzed using EDX. The variation in the Ca and P contents in the MAO coatings formed on the UFG and CG Ti substrates with different reaction times are shown in Table 1 from top views, which were mainly over a depth range of 10–20  $\mu\text{m}$ . With increasing reaction time, the amount of Ca and P increased in both substrates; however, the contents of these elements were 60% higher in the E20 than in the C20 coating.

The variations in the Ca/P atomic ratio on MAO coating formed on the UFG and CG Ti substrates with different reaction times are also shown in Table 1. The Ca/P ratio increased from 1.54 to 1.96 with reaction time increasing from 2 to 20 min in the coatings on the UFG Ti. With the same reaction time, the Ca/P ratio in the coatings formed on the CG Ti increased from 1.12 to 1.57, which is

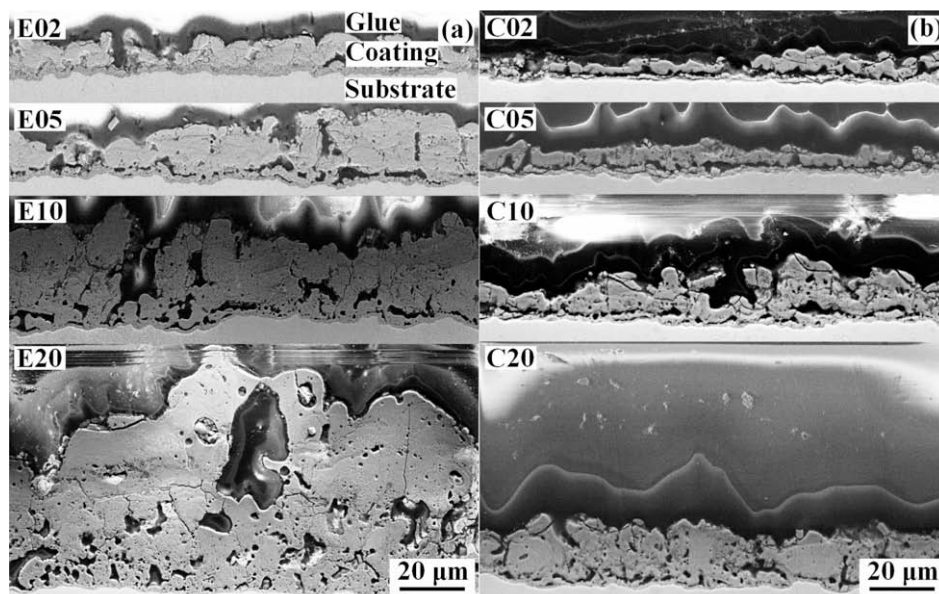


Fig. 3. Cross-sectional SEM views of MAO coatings formed on UFG Ti (a) and CG (b) Ti during different reaction times.



**Table 1**

Relative contents of Ca and P and the Ca/P ratio of the surface of MAO coating formed on UFG Ti and CG Ti.

Sample	Relative content		Ca/P ratio
	Ca (at.%)	P (at.%)	
E20	15.4 ± 0.7	7.9 ± 0.5	1.96
E10	10.6 ± 0.7	5.7 ± 0.3	1.84
E05	6.9 ± 0.4	4.4 ± 0.3	1.58
E02	5.1 ± 0.3	3.3 ± 0.2	1.54
C20	9.7 ± 0.6	6.2 ± 0.3	1.57
C10	6.4 ± 0.5	4.5 ± 0.3	1.40
C05	4.8 ± 0.3	4.1 ± 0.3	1.18
C02	4.5 ± 0.3	4.0 ± 0.2	1.12

slightly lower than that of stoichiometric HA (1.67). This indicates that the apatite formed is Ca-deficient HA on the CG Ti.

The analysis of the chemical content of the coating layers of C20, E02 and E20 samples by means of XPS is shown in Fig. 4a from a top view, in which all data are mainly from a depth range up to ~5 nm. The major surface constituents found for the MAO coating are Ca, P, O, Ti and C. Fig. 4b shows O1s XPS spectra of the surface of C20, E02 and E20 coatings. According to Refs. [37–39], the spectra can be deconvoluted into three peak components. The peak located at 530.1 eV is assigned to O1s in TiO<sub>2</sub> [38]. The second peak at 531.3 eV corresponds to O1s in P=O— [39] groups (by  $\alpha$ -Ca<sub>3</sub>(PO<sub>4</sub>) and Ca<sub>10</sub>(PO<sub>4</sub>)<sub>6</sub>(OH)<sub>2</sub>) [40]. The third peak at 532.8 eV is attributed to the contribution from O1s in basic —OH (by Ca<sub>10</sub>(PO<sub>4</sub>)<sub>6</sub>(OH)<sub>2</sub>) [37]. The relative area ratios of the three peaks are listed in Table 2.

The XPS detail spectra of Ti2p and C1s from C20, E02 and E20 are shown in Fig. 4c and d. One can see clearly that the concentra-

tion of Ti is higher on the surface of E02 than on the other samples. The elemental compositions are shown in Table 3. For the E20 sample, the concentrations of Ca and P are about 19.6% and 9.3%, giving a Ca/P ratio of about 2.1, consistent with the data obtained from the EDX. However, the Ca concentrations of E02 and C20 are 9.6% and 12.3%, respectively, with the Ca/P ratio of about 1.1, which is considerably less than that of E20.

In the C1s spectra, the predominant peak at 284.8 eV corresponds to organic carbon (C—H, C—C). The P2p peaks of the coatings are well fitted at 133.4 eV, and can be assigned to P2p in PO<sub>4</sub><sup>3-</sup> (at 133.4 eV) but not to HPO<sub>4</sub><sup>2-</sup> (at 134.4 eV) [41]. The Ca2p3/2 and Ca2p1/2 of the coatings are located at 347.5 and 351.1 eV, respectively, corresponding to Ca2p in Ca<sub>3</sub>(PO<sub>4</sub>)<sub>2</sub> and Ca<sub>10</sub>(PO<sub>4</sub>)<sub>6</sub>(OH)<sub>2</sub> [31]. The Ti2p3/2 and Ti2p1/2 XPS peaks of the coating, located at 458.5 and 464.3 eV, respectively, are well fitted to those of Ti2p in TiO<sub>2</sub> [30]. There is no influence of the chemical state of Ti, Ca and P in the C20, E02 and E20 MAO coatings.

### 3.3. Phase identification of MAO coating layers

The XRD patterns obtained from the MAO coating layers on UFG and CG Ti are shown in Fig. 5a and b, respectively. The MAO film mainly consists of two types of titanium dioxide modifications: metastable anatase and stable rutile. As the oxidizing time increased, the content of anatase phase in the coatings decreased, while the content of rutile phase increased. After 20 min, the rutile became the predominant phase in the coatings, and the anatase phase disappeared almost completely from the UFG substrate. At the same time, we still observed weak XRD peaks of the anatase phase in the C20 MAO coating (Fig. 5b). It can be inferred that

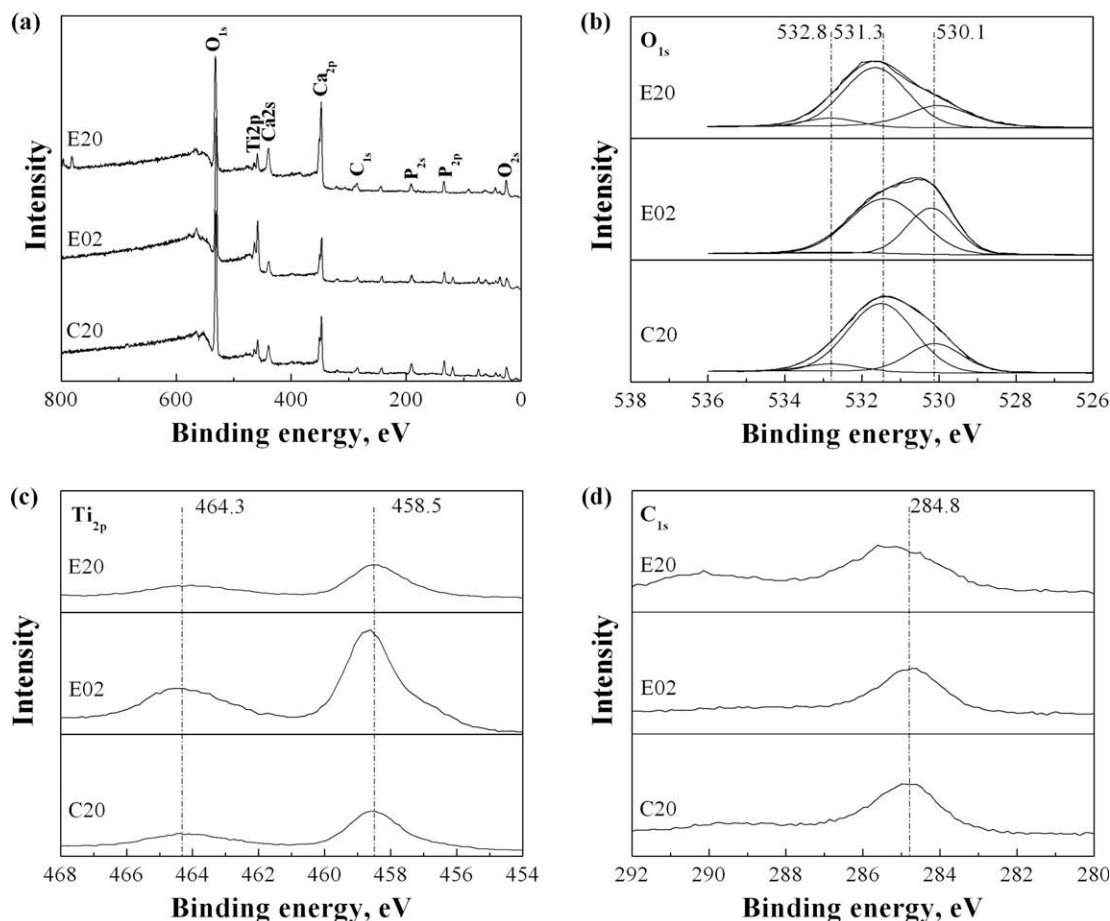


**Fig. 4.** (a) Survey spectrum, (b) O1s, (c) Ti2p and (d) C1s XPS spectra of the C20, E02 and E20 coatings.

**Table 2**

Percentage areas of the peaks obtained by deconvoluting the XPS O1s spectra of the surfaces of the C20, E02 and E20 coatings.

Sample	Percentage area of the deconvoluted peaks		
	530.1 eV	531.3 eV	532.8 eV
E20	27.9	64.2	7.9
E02	36.4	61.6	2.0
C20	26.0	67.7	6.3

**Table 3**

Elemental compositions on the surface of the MAO coatings by XPS (%) (error bars are <5%).

Samples	Elemental composition (at.%)				
	O	Ca	P	Ti	C
E20	53.6	19.6	9.3	3.6	13.9
E02	62.0	9.6	8.6	11.5	8.3
C20	61.3	12.3	11.6	4.3	10.6

the phase transformation occurs from metastable anatase into stable rutile during the MAO treatment.

After MAO treatment of ECAP-treated Ti for 10 min, the diffraction pattern from the surface of the MAO coating exhibits three weak and broad diffraction peaks at  $2\theta = 26.6^\circ$ ,  $35.9^\circ$  and  $39.9^\circ$  (see Fig. 5a). The results are close to the standard ICDD X-ray diffraction file for  $\alpha\text{-Ca}_3(\text{PO}_4)_2$  (No. 09-0348), which confirms that the coatings are composed of  $\alpha\text{-Ca}_3(\text{PO}_4)_2$  with a low crystallinity phase.

As the oxidizing time increased to 20 min, the intensity of the  $\alpha\text{-Ca}_3(\text{PO}_4)_2$  peak increased, and new peaks appeared at  $2\theta = 30.2^\circ$ ,  $37.1^\circ$ ,  $37.6^\circ$ ,  $38.4^\circ$ ,  $39.7^\circ$  and  $58.2^\circ$  (see Fig. 5a). It is suggested that HA with low-crystallinity apatite was formed. For coatings formed on the CG Ti, the diffraction peaks of  $\alpha\text{-Ca}_3(\text{PO}_4)_2$  appeared after treatment for 20 min. The intensity of peaks was close to that of E10.

Cross-sectional TEM microstructures of E20 specimens are shown in Fig. 6. Compared with the microstructure of initial ECAP-treated Ti [9], the grain size of the Ti substrate remains unchanged. A large amount of pores with a diameter of less than 200 nm can be found in the coating. From high-magnification images at the interface (as shown in Fig. 6c and d), the thickness of the dense  $\text{TiO}_2$  layer with the lower density of pores is approximately 100 nm. Fig. 6e is a dark-field micrograph of the top layer of the E20 coating. The coating is composed of a porous nanocrystalline layer (a mixture of rutile, hydroxyapatite and  $\alpha\text{-Ca}_3(\text{PO}_4)_2$  phases) with a thickness of about 2  $\mu\text{m}$  and a compacted  $\text{TiO}_2$  layer

with an average grain size of about 500 nm, together with many bubble-like pores at the grain boundaries.

### 3.4. Hardness and elastic modulus

In Fig. 7, the hardness ( $H$ ) of as-ECAP-treated Ti, ECAP-treated Ti substrates and CG Ti are exhibited. The microhardness of CG Ti increased from 1.5 to 3.1 GPa (in the extrusion direction) after the ECAP process. The microhardness of ECAP-treated Ti substrates decreased slightly with increasing reaction time. Compared with the ECAP-treated Ti, the hardness of the E20 substrate was reduced by 8% to 2.9 GPa. However, it is still considerably higher than that of pure CG Ti (about 1.5 GPa). The hardness of the whole substrate is rather homogeneous. In the region ranging from the interface to about 1  $\mu\text{m}$  across substrate of ECAP-treated Ti, the hardness changes slightly. This will be illustrated in the results of the EBSD analysis (see below).

From these results, we assume that the residual stress of the ECAP-treated Ti surface decreased remarkably and the mechanical properties of the ECAP-treated Ti sample were barely affected by the MAO process. The average values of the hardness and elastic Young's modulus of the MAO coating are about 5.1 and 74.3 GPa, respectively. The hardness of the coating is higher than that of the Ti substrate, and the elastic Young's modulus of the coating layer is lower than that of the substrate.

### 3.5. Microstructural thermal stability of ECAP-treated Ti during the MAO process

To study the thermal stability of the microstructures of the ECAP-treated Ti during the MAO process, the microstructures of the ECAP-treated sample in the regions next to the interface of E20 (in the cross-section and along the extrusion direction) were observed using EBSD (Fig. 8b). For comparison, the microstructure of the as-ECAP-treated sample is shown in Fig. 8a. After MAO treatment of ECAP-treated Ti for 20 min, no obvious change of the grain size and shape was observed by EBSD. The average grain size ( $D$ ) of the ECAP-treated sample and the E20 substrates are  $0.35 \pm 0.14$  and  $0.36 \pm 0.16$   $\mu\text{m}$ , respectively. However, in a thin layer within a distance of 1  $\mu\text{m}$  from the interface the microstructure of E20 substrate obviously changed because of the high temperature and the high pressure during the MAO process (see Fig. 8b).

### 3.6. Bioactivity of the coating layer

The surface morphologies of the specimens immersed in simulated body fluid are shown in Fig. 9. After 2 days of immersion,

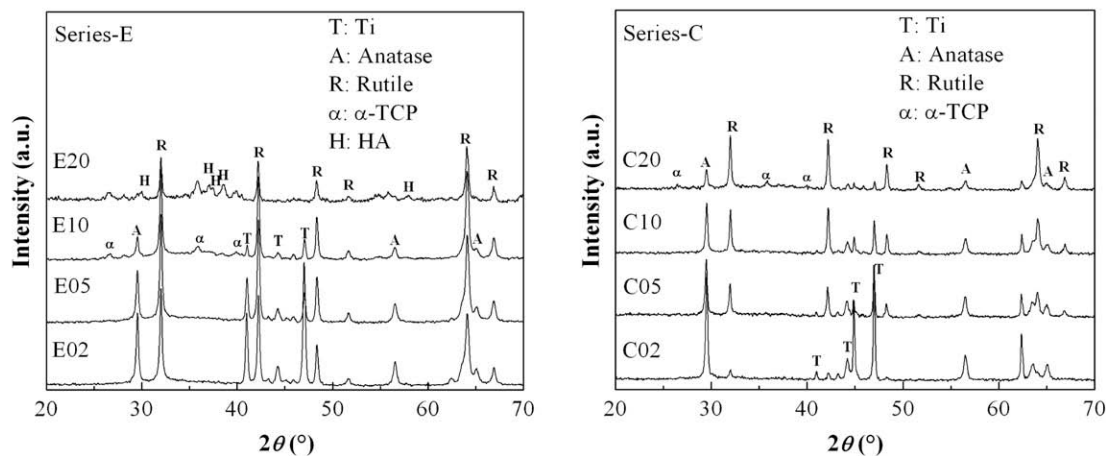
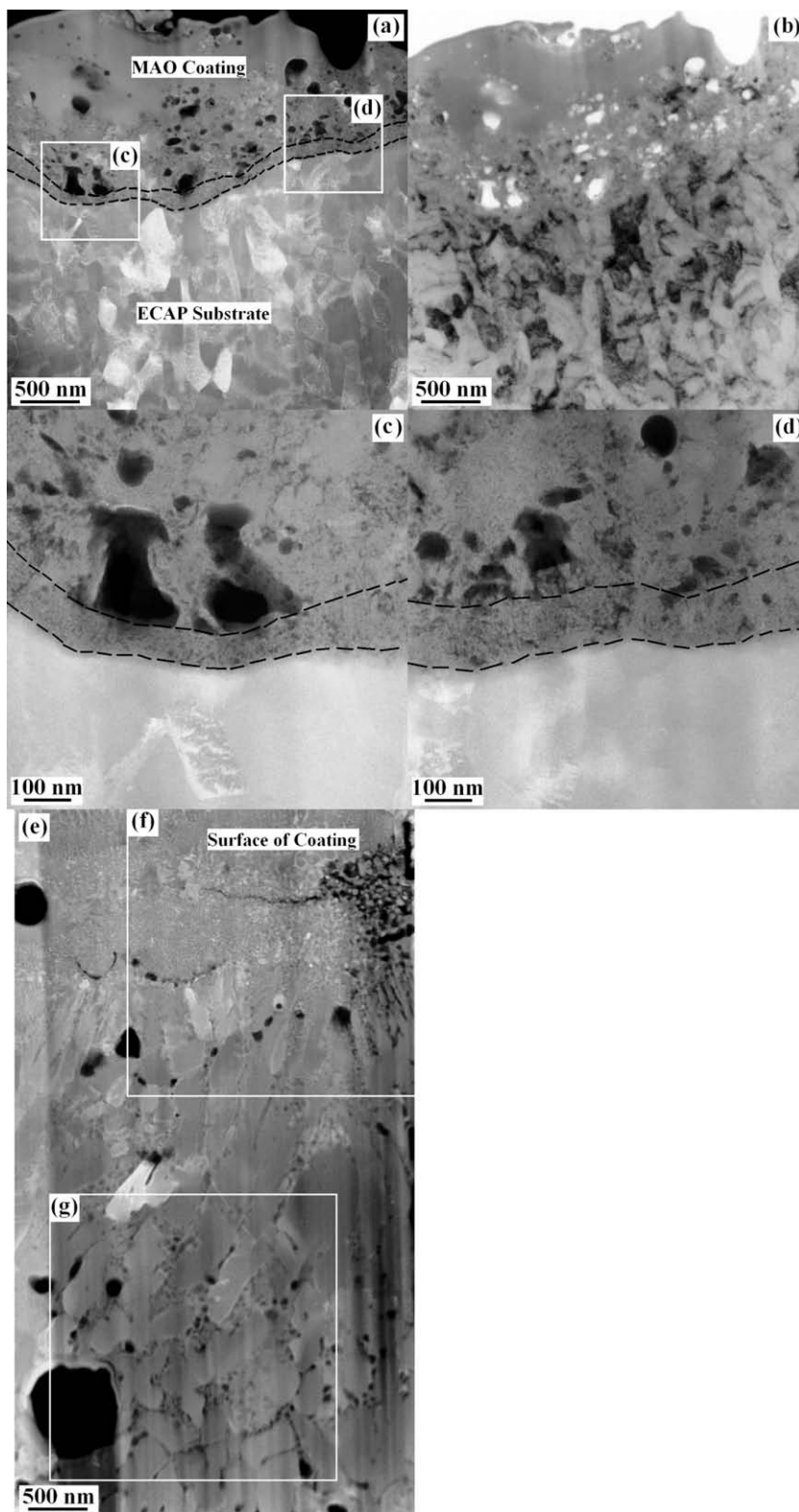


Fig. 5. XRD patterns of MAO coatings obtained on UFG Ti and CG Ti substrates in 2, 5, 10 and 20 min.



**Fig. 6.** Transmission electron micrograph of a cross-section of E20. (a) Dark-field image of E20 interface; (b) bright-field image of (a); (c and d) high-magnification images of (a); (e) dark-field image of the top layer.

carbonate-containing HA precipitates [36] appeared on the porous surface of the E10 specimen (see inset of Fig. 9c), while the entire exposed surface of the E20 specimen was covered with HA precipitates (see inset of Fig. 9d). The size of the precipitates increased with increasing immersion time, and they spread over the entire

surface. Most of the exposed surface was covered by the precipitates after 4 days of immersion, and further increasing immersion time resulted in a grain-like, smooth surface with some cracks. Carbonate-containing HA could not form on the E02, E05, C02, C05, C10 and C20 surfaces soaked in the SBF for 8 days. The Ca/P ratio



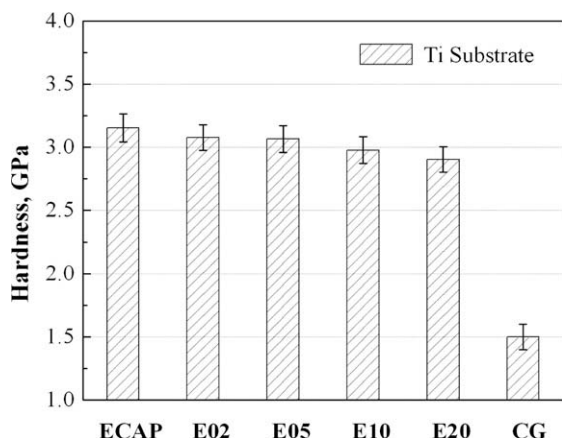


Fig. 7. Variation in hardness of the UFG Ti, CG Ti and UFG MAO substrates during different reaction times.

in the HA precipitates layer formed on the E20 surface was found to be 1.57 by means of EDX.

## 4. Discussion

### 4.1. Influence of grain refinement on the MAO process

The main parameters that influence the bioactivity of the samples with MAO coatings include: (i) the phase composition of the coating: the phases of titanium dioxide (rutile, anatase), Ca and P-containing phases (HA,  $\alpha$ - $\text{Ca}_3(\text{PO}_4)_2$ , amorphous); (ii) the contents of Ca and P, and the ratio of Ca/P; and (iii) the surface morphologies (roughness, pore size, pore density) [31,42]. Rutile, the high-temperature phase of titanium dioxide, shows greater bioactivity than the low-temperature phase, metastable anatase. In addition, the bioactivity of rutile on its (0 0 1)-crystalline plane is greater than on its other two ((1 1 0)- and (1 0 0)-) crystalline planes [43]. With increasing Ca and P contents and increasing Ca/P ratio, the bioactivity of the MAO coating was found to increase [44]. In addition, incrementation of the surface roughness and the size of pores not only improves the osteogenesis, but also enhances adhesion between the implants and the host bone. In order to further improve the biological performance of the MAO coatings, considerable efforts have been devoted to optimizing the electrical parameters, electrolyte solution, reaction duration and hydrothermal treatment [26,27,31].

In this study, we investigated the influence of the grain refinement of the ECAP-processed titanium substrate on the performance of the MAO coating. The ECAP-treated samples demonstrated an enhanced performance compared with the coarse-grained Ti samples. Therefore tailoring the microstructure of the Ti substrates through

excessive grain refinement certainly helps to accelerate the chemical reaction rate on the surface of the material.

The acceleration of the MAO process can mostly be attributed to the enhanced O, Ca and P diffusion in the non-equilibrium UFG structure. It has been demonstrated that severe plastic deformation can strongly enhance the chemical reaction (or phase transformation) kinetics thanks to the formation of a sub-microcrystalline structure with high-energy grain boundaries and other structural defects [35]. As determined by EDX and XPS, the Ca and P contents and the Ca/P ratio in the E20 coating were considerably higher than those in the C20 coating (see Tables 1 and 3). Moreover, the thickness of the E20 coating was  $58 \pm 10 \mu\text{m}$ , and was thus greater than that of C20, the thickness of which was only  $20 \pm 5 \mu\text{m}$  (see Fig 3). The Ca/P ratio in the E20 coating was found to be 1.67.

From a thermodynamic point of view, the driving force for the MAO process is enhanced for the UFG-Ti phase, which contained a large number of defects and thus stored a large excess energy. This seems to induce an extra driving force for the titanium oxide formation, the transformation from anatase to rutile and the  $\alpha$ - $\text{Ca}_3(\text{PO}_4)_2$ /HA formation process. In the E20 coating, the anatase phase mostly transformed to rutile, which has better bioactivity. In contrast, this phenomenon was not observed in the C20 coating (see Fig. 5b).

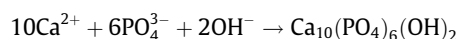
### 4.2. Thermal stability of the UFG Ti substrate during the MAO process

Due to their non-equilibrium nature UFG and nanocrystalline materials are thermally unstable. Furthermore, the MAO process is accompanied by the generation of heat due to the temperature spikes in the discharge channels [45], promoting the conversion of the Ti substrate into titania and the diffusion of Ca and P.

However, according to the hardness and EBSD results, the temperature reached in the E20 substrate can be safely estimated to be less than 300–400 °C, which is lower than the recrystallization temperature of UFG Ti. Since the thickness of the substrate was only 3 mm, the thermal effect is almost negligible, except in the zone up to 1  $\mu\text{m}$  from the interface (Fig. 8).

### 4.3. Bioactivity and mechanical properties of the MAO coating formed on ECAP-treated Ti

It is well known that the capacity of biomaterials to form HA from SBF could reflect their potential for bonding with bone. The formation of stoichiometric HA from the calcium, phosphate and hydroxyl ions can be expressed as follows [46]:



The formation process of HA crystals on the oxide film is affected by two factors: nucleation of HA and diffusion of Ca and P ions from the inner layer towards the film surface. Unlike samples E02 and E05, the MAO coating of the E10 sample contains

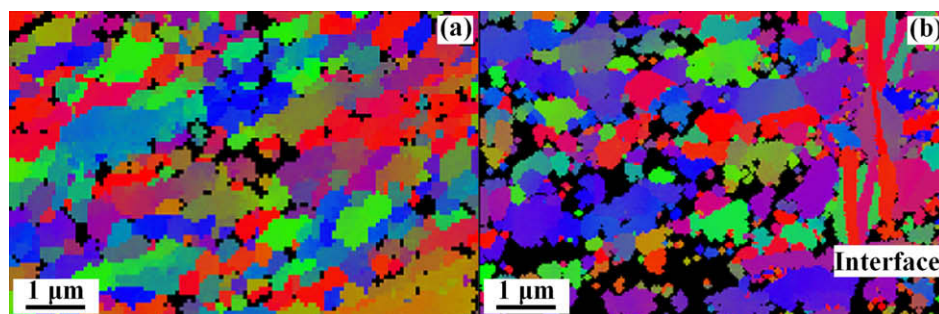
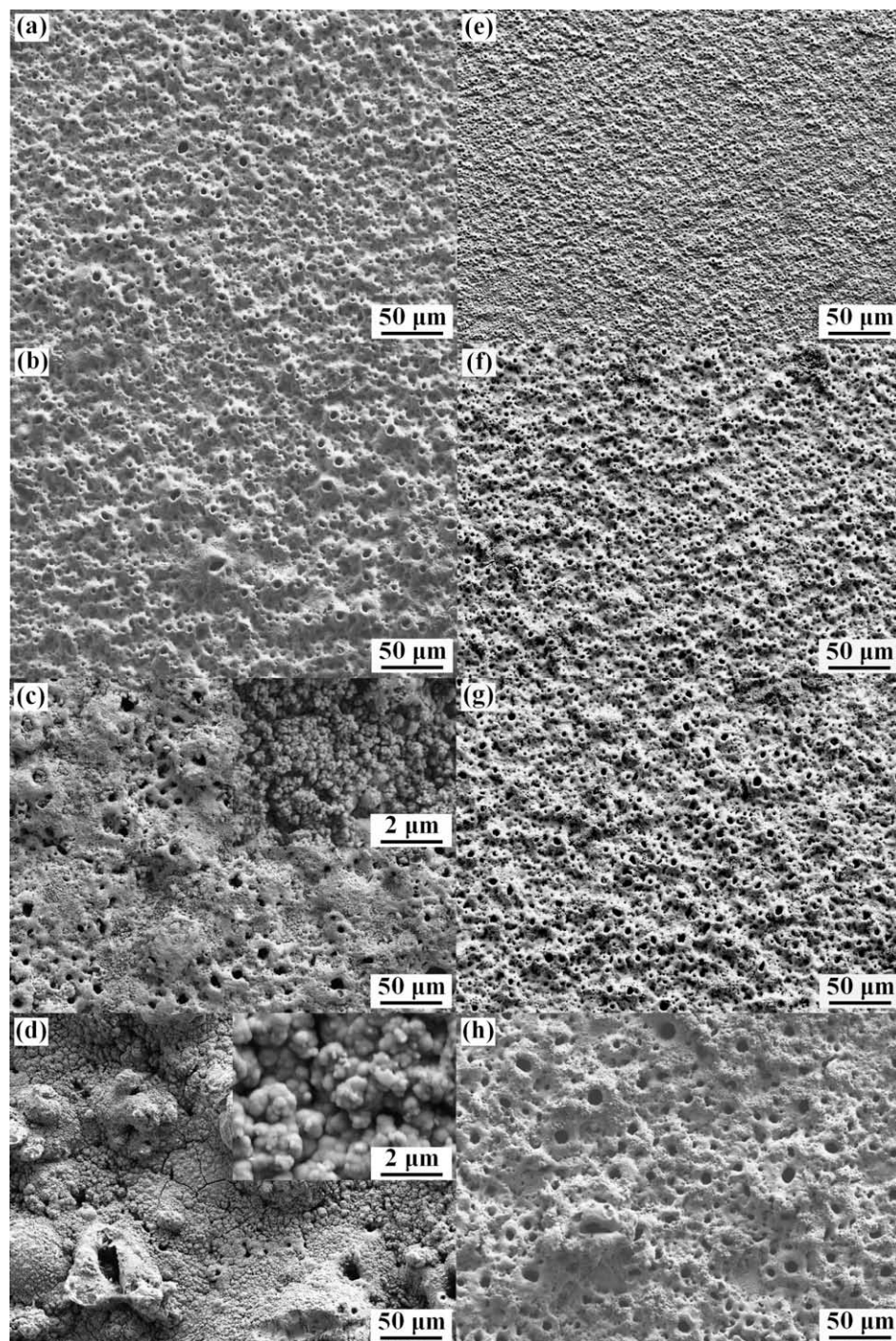


Fig. 8. The grain map and size of the ECAP-treated Ti (extrusion direction) and E20 substrate near the interface.





**Fig. 9.** Surface views of MAO coatings formed on UFG and CG Ti soaked in SBF in 2 days. (a) E02, (b) E05, (c) E10, (d) E20, (e) C02, (f) C05, (g) C10, (h) C20.

$\alpha$ - $\text{Ca}_3(\text{PO}_4)_2$  and that of the E20 sample contains both HA and  $\alpha$ - $\text{Ca}_3(\text{PO}_4)_2$  phase, which increase the nucleation rate of HA in SBF. The contents of Ca and P in the MAO coating of the E20 sample was higher than in the E10 and C20 samples. Thus, the increase in the growth rate of the apatite layer with increasing contents of HA and  $\alpha$ - $\text{Ca}_3(\text{PO}_4)_2$  and percentage composition of Ca and P ions can be attributed to the following reasons: (i) an increase in the localized initial supersaturation of the SBF with respect to apatite as more sites for HA dissolution are available; and (ii) a decrease in the incubation time needed for the initial supersaturation to be achieved. Both factors should lead to a higher ionic product of the sample E20 in solution, and consequently an increased driving

force for the formation of apatite precipitates. In addition, the increase in the surface roughness and pore sizes of E20 improves the nucleation of HA.

In the case of biomaterials for load-bearing applications, the elastic modulus is an important factor. The stiffness mismatch between the implant material and the surrounding bone leads to a “stress shielding” of the bone [47]. Higher values of stiffness or of elastic modulus of the implant will result in bone loss, bone fracture and damage of the bone surface. Compared with the CG Ti substrate, the elastic modulus of the MAO coating is close to that of natural bone (10–40 GPa) [48]. The results demonstrate that the MAO coating formed on the ECAP-treated Ti has an optimum

combination of mechanical properties and bioactivity after MAO treatment for 20 min.

## 5. Conclusions

Due to a high defect density and a large number of high-energy grain and sub-grain boundaries, the chemical reactivity of UFG Ti is significantly increased. The MAO layer thickness, roughness and diameter of discharge channel were found to increase with increasing reaction time, while the number of discharge pores decreased. The MAO coatings formed on the ECAP-treated Ti were thicker and exhibited a smaller discharge channel than the CG Ti samples after the same reaction time. The amount of Ca and P and the Ca/P ratio of the surface of the MAO coating formed on the ECAP-treated Ti is considerably higher than that of the CG Ti samples, resulting in improved bioactivity. Bone-like apatite formed quickly on the coating of the ECAP-treated Ti by incubation in SBF. The influence of reaction heat on the thermal stability of the UFG Ti substrate during the MAO process is minor and can safely be neglected while the microhardness of the substrate is reduced by about 8% to 2.9 GPa. Therefore, the results clearly demonstrate that the MAO coating formed on the ECAP-treated Ti exhibits an optimum combination of mechanical properties and bioactivity.

## Acknowledgements

Z.Y. would like to thank the China Scholarship Council (CSC) for financial support. We are grateful to A. Minkow and L. Kroner, from IMNM, Ulm University, Germany, for assistance with the SEM and XRD measurements, and Prof. S. Das, from IIT Kharagpur, India, and Dr. W. Zhao, from Ulm University, Germany, for discussions.

## Appendix. Figures with essential colour discrimination

Certain figures in this article, particularly Figure 8, are difficult to interpret in black and white. The full colour images can be found in the on-line version, at [doi: 10.1016/j.actbio.2009.12.053](https://doi.org/10.1016/j.actbio.2009.12.053).

## References

- [1] Hao YL, Li SJ, Sun BB, Sui ML, Yang R. Ductile titanium alloy with low Poisson's ratio. *Phys Rev Lett* 2007;98:216405–8.
- [2] Latysh V, Krallics G, Alexandrov I, Fodor A. Application of bulk nanostructured materials in medicine. *Curr Appl Phys* 2006;6:262–6.
- [3] Moskalik RR, Alfantazi AM. Processing of vanadium: a review. *Miner Eng* 2003;16:793–805.
- [4] Kim WJ, Hyun CY, Kim HK. Fatigue strength of ultrafine-grained pure Ti after severe plastic deformation. *Scripta Mater* 2006;54:1745–50.
- [5] Zhao YH, Liao XZ, Jin Z, Valiev RZ, Zhu YT. Microstructures and mechanical properties of ultrafine grained 7075 Al alloy processed by ECAP and their evolutions during annealing. *Acta Mater* 2004;52:4589–99.
- [6] Ivanisenko Y, Kurmanava L, Weissmueller J, Yang K, Markmann J, Roesner H, et al. Deformation mechanisms in nanocrystalline palladium at large strains. *Acta Mater* 2009;57:3391–401.
- [7] Ivanisenko Y, Valiev RZ, Fecht H-J. Grain boundary statistics in nano-structured iron produced by high pressure torsion. *Mater Sci Eng A* 2005;390:159–65.
- [8] Richtert M, Liu Q, Hansen M. Microstructural evolution over a large strain range in aluminium deformed by cyclic-extrusion-compression. *Mater Sci Eng A* 1999;260:275–83.
- [9] Stolyarov VV, Zhu YT, Alexandrov IV, Lowe TC, Valiev RZ. Grain refinement and properties of pure Ti processed by warm ECAP and cold rolling. *Mater Sci Eng A* 2003;343:43–50.
- [10] Shin DH, Kim I, Kim J, Kim YS, Semiatin SL. Microstructure development during equal-channel angular pressing of titanium. *Acta Mater* 2003;51:983–96.
- [11] Vinogradov A, Hashimoto S, Kopylov V. Enhanced strength and fatigue life of ultra-fine grain Fe–36Ni Invar alloy. *Mater Sci Eng A* 2003;355:277–85.
- [12] Sergueeva AV, Stolyarov VV, Valiev RZ, Mukherjee AK. Superplastic behaviour of ultrafine-grained Ti–6Al–4V alloys. *Mater Sci Eng A* 2002;323:318–25.
- [13] Valiev RZ, Semenova IP, Latysh VV, Rack H, Lowe TC, Petruzelka J, et al. Nanostructured titanium for biomedical applications. *Adv Eng Mater* 2008;10:15–7.
- [14] Estrin Y, Kasper C, Diederichs S, Lapovok R. Accelerated growth of preosteoblastic cells on ultrafine grained titanium. *J Biomed Mater Res* 2008;90:1239–42.
- [15] Park JW, Kim YJ, Park CH, Lee DH, Ko YG, Jang JH, et al. Enhanced osteoblast response to an equal channel angular pressing-processed pure titanium substrate with microrough surface topography. *Acta Biomater* 2009;5:3272–80.
- [16] Heimann RB, Wirth R. Formation and transformation of amorphous calcium phosphates on titanium alloy surfaces during atmospheric plasma spraying and their subsequent in vitro performance. *Biomaterials* 2006;27:823–31.
- [17] Liu XY, Chu PK, Ding CX. Surface modification of titanium, titanium alloys and related materials for biomedical applications. *Mater Sci Eng R* 2004;47:49–121.
- [18] Xie YT, Liu XY, Huang AP, Ding CX, Chu PK. Improvement of surface bioactivity on titanium by water and hydrogen plasma immersion ion implantation. *Biomaterials* 2005;26:6129–35.
- [19] Kim HW, Kim HE, Knowles JC. Fluor-hydroxyapatite sol–gel coating on titanium substrate for hard tissue implants. *Biomaterials* 2004;25:3351–8.
- [20] Cheng K, Han GR, Weng WJ, Qu HB, Du PY, Shen G, et al. Ferreira sol–gel derived fluoridated hydroxyapatite films. *Mater Res Bull* 2003;38:89–97.
- [21] Pham MT, Matz W, Reuther H, Richter E, Steiner G, Oswald S. Ion beam sensitizing of titanium surfaces to hydroxyapatite formation. *Surf Coat Technol* 2000;128–129:313–9.
- [22] Feng B, Chen JY, Qi SK, He L, Zhao JZ, Zhang XD. Carbonate apatite coating on titanium induced rapidly by precalcification. *Biomaterials* 2002;23:173–9.
- [23] Toworfe GK, Composto RJ, Shapiro IM, Ducheyne P. Nucleation and growth of calcium phosphate on amine-, carboxyl- and hydroxyl-silane self-assembled monolayers. *Biomaterials* 2006;27:631–42.
- [24] Wang YM, Liang BL, Lei TQ, Guo LX. Microarc oxidation coating formed on Ti6Al4V in Na<sub>2</sub>SiO<sub>3</sub> system solution: microstructure, mechanical and tribological properties. *Surf Coat Technol* 2006;201:82–9.
- [25] Li LH, Kong YM, Kim HW, Kim YW, Kim HE, Heo SJ, et al. Improved biological performance of Ti implants due to surface modification by micro-arc oxidation. *Biomaterials* 2004;25:2867–77.
- [26] Ryu HS, Song WH, Hong SH. Biomimetic apatite induction of P-containing titania formed by micro-arc oxidation before and after hydrothermal treatment. *Surf Coat Technol* 2008;202:1853–8.
- [27] Nie X, Leyland A, Matthews A, Jiang JC, Meletis EI. Effects of solution pH and electrical parameters on hydroxyapatite coatings deposited by a plasma-assisted electrophoresis technique. *J Biomed Mater Res* 2001;57:612–8.
- [28] Song WH, Ryu HS, Hong SH. Apatite induction on Ca-containing titania formed by micro-arc oxidation. *J Am Ceram Soc* 2005;88:2642–4.
- [29] Matykina E, Arrabal R, Skeldon P, Thompson GE. Transmission electron microscopy of coatings formed by plasma electrolytic oxidation of titanium. *Acta Biomater* 2009;5:1356–66.
- [30] Frauchiger VM, Schlottig F, Gasser B, Textor M. Anodic plasma-chemical treatment of CP titanium surfaces for biomedical applications. *Biomaterials* 2004;25:593–606.
- [31] Song WH, Jun YK, Han Y, Hong SH. Biomimetic apatite coating on micro-arc oxidized titania. *Biomaterials* 2004;25:3341–9.
- [32] Han Y, Sun J, Huang X. Formation mechanism of HA-based coatings by micro-arc oxidation. *Electrochem Commun* 2008;10:510–3.
- [33] Wei DQ, Zhou Y, Jia DC, Wang YM. Characteristic and in vitro bioactivity of a microarc-oxidized TiO<sub>2</sub>-based coating after chemical treatment. *Acta Biomater* 2007;3:817–27.
- [34] Kim DY, Kim M, Kim HE, Koh YH, Kim HW, Jang JH. Formation of hydroxyapatite within porous TiO<sub>2</sub> layer by micro-arc oxidation coupled with electrophoretic deposition. *Acta Biomater* 2009;5:2196–205.
- [35] Tong WP, Tao NR, Wang ZB, Lu J, Lu K. Nitriding iron at lower temperatures. *Science* 2003;299:686–8.
- [36] Kokubo T, Takadama H. How useful is SBF in predicting in vivo bone biocompatibility? *Biomaterials* 2006;27:2907–15.
- [37] Kasuga T, Kondo H, Nogami M. Apatite formation on TiO<sub>2</sub> in simulated body fluid. *J Cryst Growth* 2002;235:235–40.
- [38] Sham TK, Lazarus MS. X-ray photoelectron spectroscopy (XPS) studies of clean and hydrated TiO<sub>2</sub> (rutile) surfaces. *Chem Phys Lett* 1979;68:426–32.
- [39] Dupraz A, Nguyen TP, Richard M, Daculsi G, Passuti N. Influence of a cellulosic ether carrier on the structure of biphasic calcium phosphate ceramic particles in an injectable composite material. *Biomaterials* 1999;20:663–73.
- [40] Zhu XL, Chen J, Scheideler L, Reichl R, Geis-Gerstoefer J. Effects of topography and composition of titanium surface oxides on osteoblast responses. *Biomaterials* 2004;25:4087–103.
- [41] Viornery C, Chevolut Y, Leonard D, Aronsson BO, Pechy P, Mathieu HJ, et al. Surface modification of titanium with phosphonic acid to improve bone bonding: characterization by XPS and ToF-SIMS. *Langmuir* 2002;18:2582–9.
- [42] Yang BC, Uchida M, Kim HM, Zhang XD, Kokubo T. Preparation of bioactive titanium metal via anodic oxidation treatment. *Biomaterials* 2004;25:1003–10.
- [43] Lindberg F, Heinrichs J, Ericson F, Thomsen P, Engqvist H. Hydroxylapatite growth on single-crystal rutile substrates. *Biomaterials* 2008;29:3317–23.
- [44] Han Y, Hong SH, Xu KW. Structure and in vitro bioactivity of titania-based films by micro-arc oxidation. *Surf Coat Technol* 2003;168:249–58.
- [45] Yerokhin AL, Nie X, Leyland A, Matthews A, Dowey SJ. Plasma electrolysis for surface engineering. *Surf Coat Technol* 1999;122:73–93.
- [46] Dorozhkin SV, Epple M. Biological and medical significance of calcium phosphates. *Angew Chem Int Ed* 2002;41:3130–46.
- [47] Ramakrishna S, Mayer J, Wintmannel E, Leong Kam W. Biomedical applications of polymer-composite materials: a review. *Compos Sci Technol* 2001;61:1189–224.
- [48] Meyers MA, Chen PY, Lin AY, Seki Y. Biological materials: structure and mechanical properties. *Prog Mater Sci* 2008;53:1–206.